Transition from the collective to the single-particle regimes in a quantum fluid

A. Cunsolo,[1] G. Monaco,[2] M. Nardone,[1] G. Pratesi,[3] and R. Verbeni[2]
[1]*Istituto Nazionale di Fisica della Materia and Universitá dell'Aquila, L'Aquila, Italy*
[2]*European Synchrotron Radiation Facility. B.P. 220 F-38043 Grenoble Cedex, France*
[3]*Istituto Nazionale di Fisica della Materia, I-50139, Firenze, Italy*
(Received 22 July 2002; revised manuscript received 28 October 2002; published 17 January 2003)

The evolution of the dynamic structure factor $S(q,\omega)$ of liquid Ne with exchanged momentum q and frequency ω has been studied by inelastic x-ray scattering in the q range extending from 0.3 to 16 Å^{-1}, i.e., covering the whole transition region from the collective regime to the single-particle one. The values of the first three spectral moments are extracted from the experiment either by direct line shape integration of the spectra or as a result of line shape best fitting procedures. The q dependence of different ratios constructed using the measured spectral moments clearly shows the transition from a classical regime, characteristic of the low-q macroscopic limit, to a quantum one, reached in the high-q microscopic limit. Moreover, direct information on the values of physically relevant parameters such as the mean atomic kinetic energy and the kinetic structure function is derived.

DOI: 10.1103/PhysRevB.67.024507 PACS number(s): 67.20.+k, 61.10.Eq, 61.20.Ja, 78.70.Ck

I. INTRODUCTION

The study of the microscopic dynamics of quantum fluids has been so far a typical domain of the deep inelastic neutron scattering (DINS) technique, which investigates the so-called impulse approximation (IA) region.[1] In this extreme portion of the q-ω plane the interaction time between probe and target is so short that the investigated dynamical process is basically the free recoil of the target particle after the collision event. Under these conditions the spectral density carries direct information on the single-particle initial momentum distribution. Many systems have been studied in this extremely-high-q regime using DINS, among them being ^{4}He,[2] H_2,[3] pyrolitic graphite,[4] simple metals,[5] and H_2S.[6]

On accessing to lower and lower q's and ω's, the interactions of the target particle with its neighbors have an increasing weight which becomes dominant close to the hydrodynamic regime.[7] In this regime, the spectral density is dominated by the characteristic features associated with the propagation of longitudinal acoustic modes and to the diffusion of heat.[7]

In general, it is very demanding to explore, on the same sample, the whole $(q,\ \omega)$ transition region extending between the single-particle and hydrodynamic regimes mainly owing to the lack of a single spectrometer allowing one to cover the whole dynamic range of interest.

Recently, a technique complementary to inelastic neutron scattering, inelastic x-ray scattering (IXS), has been thoroughly employed to study the atomic dynamics in liquids in the region where the longitudinal acoustic modes still have a propagating nature.[9] In an IXS experiment the scattering cross section is proportional to the dynamic structure factor $S(q,\omega)$, just as in a *coherent* neutron scattering experiment. Moreover, as compared to neutron scattering, the IXS technique can cover a larger dynamical range at low q thanks to the absence of kinematic limitations in the scattering of photons from matter. At high q's, conversely, IXS suffers from the intrinsic limitation of a weak cross section (see Sec. III A). Nonetheless, the x-ray fluxes available nowadays at third-generation synchrotron sources have allowed for a successful experimental study of a classical liquid system, liquid Li, over a broad $(q,\ \omega)$ range extending between the hydrodynamic and the single-particle regimes.[10]

In the present paper we follow the same route to study the atomic dynamics of liquid Ne, the prototype system for weakly quantum liquids. More specifically we study, as in the case of Li,[10] the entire evolution of the dynamic structure factor between the hydrodynamic and the single-particle limits, thus extending towards lower q values the range explored in previous neutron measurements.[11–14] In particular, we focus our attention on the derivation of a typical single-particle parameter as the mean atomic kinetic energy.[15] In this respect, it is worthwhile mentioning a recent IXS study,[16] aiming to investigate the quantum effects on the dynamics of He at low and intermediate q's. There, a method was presented which, based on the study of the q dependence at low q's of the spectral moments, provides quantitative information even on single-particle properties such as the mean atomic kinetic energy. Such a quantity is indeed usually derived from high-q experiments in the framework of the impulse approximation. Here we propose an extension of that work which can be logically split into two steps. The first step consists of a study of quantum effects in liquid Ne in the low-q range, exploiting the aforementioned technique of spectral moments.[16] As a second step, we analyze IXS spectra collected at high q's, where the impulse approximation starts to hold, and the spectral moments are derived using a method already used in neutron scattering (Ref. 14) and IXS (Ref. 17) data analyses. The entire analysis then covers a broad q range and allows us to discuss how quantum effects differently affect collective and single-particle features characteristic of the low- and high-q limits, respectively.

II. EXPERIMENT

The experiment has been carried out at the very-high-energy-resolution IXS beamline ID16 of the European Synchrotron Radiation Facility. At this beamline, a high-

resolution Si monochromator in close to backscattering geometry is used to monochromatize the synchrotron x-ray beam used in the scattering experiment. The radiation scattered by the sample is then collected in a spectrometer arm which can be rotated around the sample stage, thus selecting the scattering angle ϑ and consequently the exchanged wave number q, being $q=(4\pi/\lambda)\sin\vartheta/2$, where λ is the wavelength of the incoming x-ray beam. The analysis in energy of the scattered radiation is achieved by means of spherical Si analyzers which are used at the same reflection order as the monochromator and which focus the radiation onto Peltier-cooled Si diode detectors. The energy scans are performed by scanning the temperature of the monochromator with respect to that of the analyzer. The beamline is described in further details elsewhere.[18] Different reflections for monochromator and analyzer and different spectrometer arms were used in order to optimize the setup in the low- and high-q regions, respectively.

The thermodynamic point at which the measurements on liquid Ne were carried out is defined by a temperature of (27.6 ± 0.1) K and a pressure of (1.4 ± 0.2) bar, corresponding to a density of ≈ 0.0358 atoms/Å^3.[19]

A. Setup I: The low-q region

In this region a high resolution in both energy and momentum is required. The undulator source is tuned to the energy corresponding to the Si (11,11,11) Bragg reflection for the monochromator, i.e., $E=21.747$ keV. The spectrometer is a 6.5-m-long arm which can be rotated in the horizontal plane. Five independent analyzers are mounted in the spectrometer arm, at a constant angular offset one from the other, so to allow for the simultaneous collection of five spectra at different q's (experimental setup I).

The instrumental resolution has been obtained by measuring the spectral density of a Plexiglas sample at a q value corresponding to its first sharp diffraction peak ($q \approx 1$ Å^{-1}). In this configuration, the inelastic signal can indeed be considered to be completely negligible as compared to the resolution-broadened elastic one. The obtained resolution profile has an almost Lorentzian shape with a full width at half maximum (FWHM) of (1.5 ± 0.1) meV for each of the five analyzers. The q resolution was set to 0.035 Å^{-1} FWHM. The q range studied using this configuration extends from 0.3 to 3.05 Å^{-1}, thus including the region of the first sharp diffraction maximum at $q_m \approx 2.35$ Å^{-1} for liquid Ne. Each spectrum was obtained by summing up three energy scans, extending typically from -20 meV to 35 meV and lasting about 200 min each.

The Ne sample was condensed in a cylindrical hole drilled in a copper plate and enclosed between two single-crystal diamond disks (0.5 mm thickness and 4 mm diameter) which are the windows for the incoming beam and for the (almost) forward-scattered radiation. The distance between the two diamond windows, i.e., the sample length along the beam, was 10 mm, which roughly matches the photoelectric absorption length of Ne at the considered energy. The sample holder was kept under vacuum and in thermal contact with a closed-cycle cryostatic refrigerator.

B. Setup II: The high-q region

In this region, less stringent requirements on both the energy and the momentum resolutions can be accepted. The undulator source was tuned to the energy corresponding to the Si (9,9,9) Bragg reflection for the monochromator, i.e., $E=17.793$ keV. The spectrometer is a 2.5-m-long arm which can be rotated in the vertical plane up to a maximum scattering angle of $\approx 130°$. In the present experiment, this has allowed us to investigate q values up to 16 Å^{-1}. This vertical arm is equipped with a single analyzer.

This setup (experimental setup II), as compared with the one used for the low-q region, is characterized by a higher photon flux on the sample and an overall instrumental resolution of 6.9 meV FWHM. The latter has been obtained experimentally from the spectral density of a liquid nitrogen sample measured at the temperature of 66.4 K, pressure of 0.25 bar, and $q \simeq 1.9$ Å^{-1} (close to the first sharp diffraction peak), where it behaves as an almost elastic scatterer[20] all over the energy transfer region spanned in a typical high-q spectrum (-90 meV$\leqslant \hbar\omega \leqslant 145$ meV).

In this case the sample cell was a 7.5-mm-internal-diameter 0.25-mm-thick Plexiglas tube. Each spectrum lasted from 130 to 540 min, depending on the q value.

For both the low- and high-q experiments, the intensity scattered by the empty cell was measured and subtracted from the spectra. Corrections due to multiple scattering contributions, depending on the details of the sample shape and spectrometer optics, have been estimated following a procedure similar to the one already described in the literature.[21] Since they were found to be less than 2%, they have been neglected. This consideration makes us confident that, once the empty cell contribution is subtracted, the measured spectra are proportional to the convolution of $S(q,\omega)$ with the experimental resolution function (see Sec. III A).

Examples of typical raw IXS spectra are reported in Fig. 1(a) for the low-q configuration and in Fig. 1(b) for the high-q one. Notice the asymmetric shoulders in the low-q spectrum arising from propagating density fluctuations. In the insets, the same spectra are reported on a logarithmic scale. The vertical dashed line marks the zero-energy transfer position. A larger selection of measured spectra showing the evolution with q and the corresponding points of the structure factor $S(q)$ (Ref. 22) is reported in Fig. 2. As q is increased, the spectral line shape progressively transforms towards a single featureless band whose position moves systematically towards higher energy transfers.

III. THEORETICAL BACKGROUND AND DATA ANALYSIS

A. IXS cross section

In an IXS experiment, the probe-target interaction occurs via the electromagnetic coupling between the incoming x rays and the electrons of the target system. At small exchanged energies the spectrum of the scattered x rays reflects the dynamics of the electrons which follows adiabatically that of the nuclei.[23] Specifically, for the case of a monatomic target system, the nonresonant IXS cross section per unit exchanged frequency interval and unit solid angle Ω can be written as:[23]

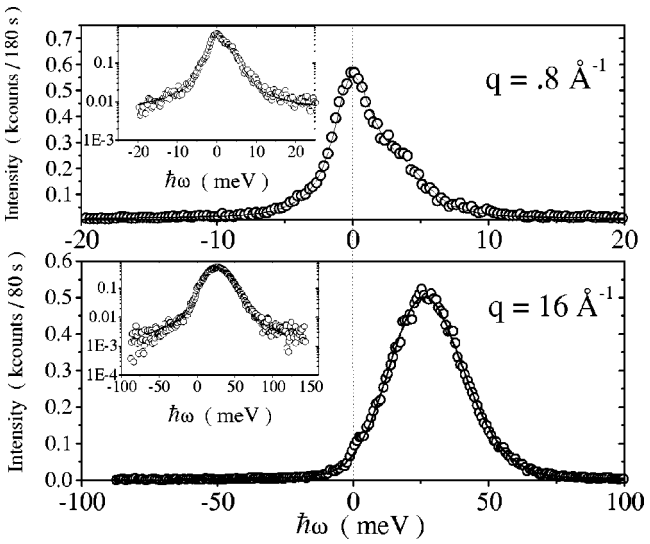

FIG. 1. The panels report two typical IXS spectra collected at low and high q (upper and lower panels, respectively). The raw data (open circles) are plotted with the best fit line shapes (solid lines) obtained using the model in Eqs. (14) and (18) (upper panel) and in Eqs. (21) and (22) (lower panel). The two inset pictures report the same data in logarithmic scale.

$$\frac{\partial^2\sigma}{\partial\omega\partial\Omega}=r_0^2|\epsilon_i\cdot\epsilon_f|^2\frac{k_i}{k_f}|f(q)|^2S(q,\omega). \tag{1}$$

Here r_0 is the classical electron radius, $\boldsymbol{\epsilon}$ and $\mathbf{k}$ are the polarization and wave vector of the incident (subscript i) and scattered (subscript f) radiation, q is the wave vector exchanged by the incident photon in the scattering process, $f(q)$ is the atomic form factor (given by the space Fourier transform of the atomic electronic density distribution), and $S(q,\omega)$ is the dynamic structure factor (given by the space-time Fourier transform of the atomic density-density correlation function). It is easy to recognize that, in the considered energy range, the IXS cross section has the same structure as the coherent neutron scattering one.[24]

B. Spectral moments

Let us define the spectral moment of $S(q,\omega)$ of order n as

$$\hbar^n\langle\omega^n\rangle=\hbar^n\int_{-\infty}^{\infty}\omega^nS(q,\omega)d\omega. \tag{2}$$

The first two moments are the zeroth spectral moment yielding directly the structure factor

$$\langle\omega^0(q)\rangle=\int_{-\infty}^{\infty}S(q,\omega)d\omega=S(q), \tag{3}$$

and the first moment which is given by the well-known exact f-sum rule, which yields

$$\hbar\langle\omega^1(q)\rangle=\frac{\hbar^2q^2}{2M}=\hbar\omega_r. \tag{4}$$

Here, M is the mass of the target atom and ω_r the recoil frequency. The first moment obviously vanishes in the classical limit.

While in principle both these moments can be used to normalize the scattering data, in the following we will adopt—for the low-q data—the normalization based on the first moment since this procedure requires only knowledge of the atomic mass M. The high-q data ($q\geq 6$ Å^{-1}) will be conversely normalized to the zeroth moment, namely to unity since, at these q values, the incoherent approximation can be considered to be valid.[14]

Moreover, following Ref. 25 (see also Ref. 26) we can easily write down an explicit expression for the second-moment ratio $R_2(q)$,

$$R_2(q)=\frac{\hbar^2\langle\omega^2(q)\rangle}{\hbar\langle\omega^1(q)\rangle}=\hbar\omega_r[2-S(q)]+\frac{2\hbar^2}{M}D(q), \tag{5}$$

where the kinetic structure function $D(q)$ can be written as[27]

$$D(q)=\frac{M}{2\hbar^2}\left[\frac{4}{3}\langle\mathrm{KE}\rangle+\Lambda(q)\right]. \tag{6}$$

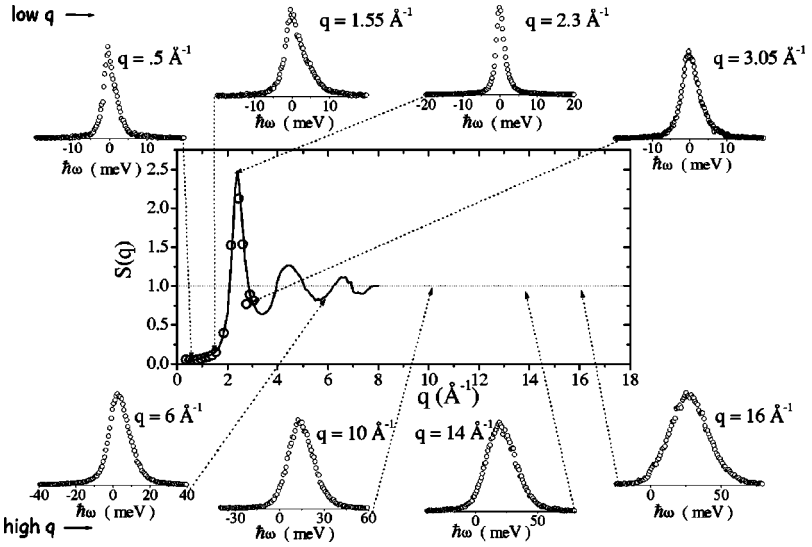

FIG. 2. The central panel reports the static structure factor as obtained through Eq. (3) from direct integration of the IXS spectral intensity (open circles) and from a neutron diffraction measurement (solid line, from Ref. 22). The plots around the central one give a schematic overview of the overall q evolution of the IXS spectral density for some representative q's.

Here $\langle \mathrm{KE} \rangle$ is the (quantum mechanically correct) average single particle kinetic energy, and $\Lambda(q)$ (Ref. 27) denotes a purely quantum contribution due to correlations between different particles which is given by

$$\Lambda(q) = \frac{1}{NM} \left\langle \sum_{i \neq j} p_i p_j \cos(q \cdot r_{ij}) \right\rangle. \tag{7}$$

Here, the sums run over the N atoms in the system, p_i being the momentum of the ith atom and r_{ij} the distance between the ith and jth atoms. Obviously $R_2(q)$ can also be defined in the classical limit, Eq. (5) being in this case[7]

$$R_2^C(q) = \frac{\langle \omega^2(q) \rangle}{q^2} 2M = \frac{4}{3} \langle \mathrm{KE} \rangle_C = 2K_B T. \tag{8}$$

Here, $\langle \mathrm{KE} \rangle_C$ is the classical kinetic energy. We notice that in the high-q limit, since $\Lambda(q \to \infty) = 0$ and $S(q \to \infty) = 1$, we have

$$\lim_{q \to \infty} [R_2(q) - \hbar \omega_r] = \frac{4}{3} \langle \mathrm{KE} \rangle, \tag{9}$$

while, in the low-q limit,

$$\lim_{q \to 0} R_2(q) = \frac{2\hbar^2}{M} D(0) = \frac{4}{3} \langle \mathrm{KE} \rangle + \Lambda(0). \tag{10}$$

For a moderately quantum fluid such as Ne in our thermodynamic conditions we can neglect exchange effects by treating the atoms as distinguishable Boltzmann particles,[8] thus obtaining

$$\lim_{q \to 0} R_2(q) = \lim_{q \to 0} R_2^C(q) = \frac{4}{3} \langle \mathrm{KE} \rangle_C = 2K_B T. \tag{11}$$

Finally, using the expression of the third spectral moment derived under the assumption of a pairwise additive interatomic potential $\phi(r)$, we can also define a third-moment ratio $R_3(q)$ given by[28]

$$R_3(q) = \frac{\hbar^3 \langle \omega^3(q) \rangle}{\hbar \langle \omega^1(q) \rangle} = (\hbar \omega_r)^2 + 4(\hbar \omega_r) \langle \mathrm{KE} \rangle + \hbar^2 (\Omega_0^2 - \Omega_q^2), \tag{12}$$

where Ω_0^2 and Ω_q^2 in Eq. (12) can be explicitly written in terms of the pair distribution function $g(r)$ and the pair potential $\phi(r)$:

$$\Omega_q^2 = \frac{\rho}{M} \int g(r) \cos(\vec{q} \cdot \vec{r}) \frac{\partial^2}{\partial z^2} \phi(r) d\vec{r},$$

$$\Omega_0^2 = \lim_{q \to 0} \Omega_q^2 = \frac{\rho}{M} \int g(r) \frac{\partial^2}{\partial z^2} \phi(r) d\vec{r} = \frac{\rho}{3M} \langle \nabla^2 \phi(r) \rangle. \tag{13}$$

Here ρ is the number density and z is the Cartesian coordinate along the axis parallel to $\vec{q}$. While Ω_q^2 vanishes at high q, the quantity Ω_0^2 is a constant generally referred to as the square of the Einstein frequency of the fluid. As a consequence,

$$\lim_{q \to \infty} [R_3(q) - 4\hbar \omega_r \langle \mathrm{KE} \rangle - \hbar^2 \omega_r^2] = \hbar^2 \Omega_0^2,$$

$$\lim_{q \to 0} R_3(q) = 0.$$

Obviously the ratio $R_3(q)$ cannot be defined in the classical limit.

C. Low-q region line shape

The model line shape adopted in the low-q region analysis is based on the classical viscoelastic model for liquids,[29] following which

$$S_C(q,\omega) = S_C(q) \frac{1}{\pi} \frac{\omega_0^2 \tau (\omega_\infty^2 - \omega_0^2)}{[\tau \omega (\omega^2 - \omega_\infty^2)]^2 + (\omega^2 - \omega_0^2)^2}, \tag{14}$$

where τ, ω_0^2, and ω_∞^2 are three q-dependent parameters representing the generalized Maxwell relaxation time and the zero- and infinite-frequency limits of the acoustic frequency, respectively. In particular, ω_0^2 and ω_∞^2 are related to the spectral moments of $S_C(q,\omega)$ by[29]

$$\omega_\infty^2 = \frac{\int_{-\infty}^{\infty} \omega^4 S_C(q,\omega) d\omega}{\int_{-\infty}^{\infty} \omega^2 S_C(q,\omega) d\omega}, \tag{15}$$

$$\omega_0^2 = \frac{\int_{-\infty}^{\infty} \omega^2 S_C(q,\omega) d\omega}{\int_{-\infty}^{\infty} S_C(q,\omega) d\omega}. \tag{16}$$

The detailed balance asymmetry of the spectra is taken into account by assuming that the imaginary part of the ''correct'' susceptibility $\chi_M''(\mathbf{q},\omega)$ of the quantum case is well represented by that corresponding to the classical model, Eq. (14), $\chi_C''(\mathbf{q},\omega)$, thus obtaining

$$\chi_C''(\mathbf{q},\omega) = \frac{\pi \omega}{K_B T} S_C(\mathbf{q},\omega) = \chi_M''(\mathbf{q},\omega) = \frac{\pi}{\hbar} [1 + n(\omega)]^{-1} S_M(\mathbf{q},\omega), \tag{17}$$

and therefore

$$S_M(q,\omega) = \frac{\hbar \omega}{K_B T} [n(\omega) + 1] S_C(q,\omega), \tag{18}$$

where $n(\omega)$ is the usual Bose-Einstein population factor.

This assumption, usually referred to as the high-temperature susceptibility limit, introduces a relationship between the odd moments of $S_M(q,\omega)$ and the even ones of $S_C(q,\omega)$:

$$\int_{-\infty}^{\infty}\omega^{2n-1}S_M(q,\omega)d\omega=\frac{\hbar}{2K_BT}\int_{-\infty}^{\infty}\omega^{2n}S_C(q,\omega)d\omega. \tag{19}$$

This implies in particular that, within the accuracy of the model, the parameter ω_∞^2 can be used to obtain the moment ratio R_3, being, for $n=2$,

$$R_3=\hbar^2\frac{\int_{-\infty}^{\infty}\omega^4S_C(q,\omega)d\omega}{\int_{-\infty}^{\infty}\omega^2S_C(q,\omega)d\omega}=\hbar^2\omega_\infty^2. \tag{20}$$

D. High-q region line shape

As previously stated, at high-q values the IA regime is reached asymptotically. In this approximation the target dynamics is probed over such a short time that the tagged particle after the collision with the probe has no time to experience any interaction with its neighbors. Clearly, before this extreme limit is reached, the struck atom does not stream freely because the interactions with its neighbors still have a role which is not entirely negligible. In such a case, the dynamic response does not simply mirror the initial-state momentum distribution, as in the IA regime, and the so-called final-state effects have to be considered. From a theoretical point of view different approaches can be followed to handle the final-state effect contributions in the $S(q,\omega)$. Hereafter we deal with the so-called additive approach[30] which stems from a cumulant time expansion of the intermediate scattering function. Retaining only the first three leading terms of such an expansion and after Fourier transforming, the following formal expression can be obtained:

$$S(q,\omega)\simeq S_G(q,\omega)+S_1(q,\omega)+S_2(q,\omega), \tag{21}$$

where $S_G(q,\omega)$ is the dominating Gaussian contribution and $S_1(q,\omega)$ and $S_2(q,\omega)$ are the first two correction terms explicitly given, in the incoherent approximation limit, by

$$S_G(q,\omega)=\frac{1}{\sqrt{2\pi\mu_2}}\exp\left[-\frac{\hbar^2\omega_d^2}{2\mu_2}\right],$$

$$S_1(q,\omega)=-\frac{\mu_3}{8\mu_2^2}\hbar\omega_d\left(1-\frac{\hbar^2\omega_d^2}{3\mu_2}\right)S_G(q,\omega),$$

$$S_2(q,\omega)=\frac{\mu_4}{8\mu_2^2}\left(1-\frac{2\hbar^2\omega_d^2}{\mu_2}+\frac{\hbar^4\omega_d^4}{3\mu_2^2S_G(q,\omega)}\right). \tag{22}$$

Here $\omega_d^2=[(\omega-\omega_r)^2]$ and $\mu_{2,3,4}$ are given by

$$\mu_2=\frac{4}{3}\hbar\omega_r\langle\mathrm{KE}\rangle=\hbar\omega_r\lim_{q\to\infty}[R_2-\hbar\omega_r],$$

$$\mu_3=\hbar^3\omega_r\Omega_0^2=\hbar\omega_r\lim_{q\to\infty}[R_3-4\hbar\omega_r\langle\mathrm{KE}\rangle-\hbar^2\omega_r^2],$$

$$\mu_4=\frac{\hbar^2q^2}{M^2}\langle F_q^2\rangle+\frac{\hbar^8q^4}{M^4}\hat{\alpha}_4. \tag{23}$$

Here $\hat{\alpha}_4=\langle p_q^4\rangle-3\langle p_q^2\rangle$ and F_q and p_q are the components along $\vec{q}$ of the force acting on the atom and of its momentum, respectively. It is evident that while μ_2 yields directly R_2, the parameter μ_3 can be used to yield an experimental determination for R_3 once the kinetic energy is derived from μ_2 and recalling that in the incoherent limit $\Omega_q^2=0$.

E. Fitting procedure

The experimental data have been fitted using a χ^2 minimization and accounting for the experimentally measured instrumental resolution function $R(\omega)$, a constant background B and a q-dependent intensity factor A along with the appropriate model line shape. In practice we have used the following function:

$$f(q,\omega)=A\cdot R(\omega)\otimes S(Q,\omega)+B, \tag{24}$$

where $\otimes$ indicates a convolution integral and $S(Q,\omega)$ is a model for the dynamical structure factor.

In particular for the spectra collected using the low-q setup (I), i.e., for $q\leqslant 3.05$ Å^{-1}, we have used the quantum-corrected viscoelastic model $S_M(q,\omega)$ of Eqs. (14) and (18), with A, B, τ, ω_0^2, and ω_∞^2 as free fitting parameters, while for the spectra collected using the high-q setup (II), i.e., for $q\geqslant 6$ Å^{-1}, we have used the cumulant expansion of Eqs. (21) and (22), with A, B, ω_r, μ_2, μ_3, and μ_4 as free fitting parameters.

IV. RESULTS AND DISCUSSION

Two examples of best fit line shapes for low- and high-q spectra are reported in Fig. 1. In the two insets we also report the same figures in logarithmic scale in order to put emphasis on the quality of the fits even in the tails of spectra.

The best fit line shapes have been used to extract by numerical integration the first and second spectral moments which, in the low-q region, are not directly related to the model fit parameters. The integration is performed directly on the model function as shown in Fig. 3 where we report, for a typical spectrum, together with the experimental spectrum and its best fit function [Fig. 3(a)], the deconvoluted model function obtained from the best fit parameters [Fig. 3(b)], and the cumulative integral of order 2 [Fig. 3(c)] as given by

$$I_2(\omega)=\hbar^2\int_{-\infty}^{\omega}\omega'^2S_M(q,\omega')d\omega'. \tag{25}$$

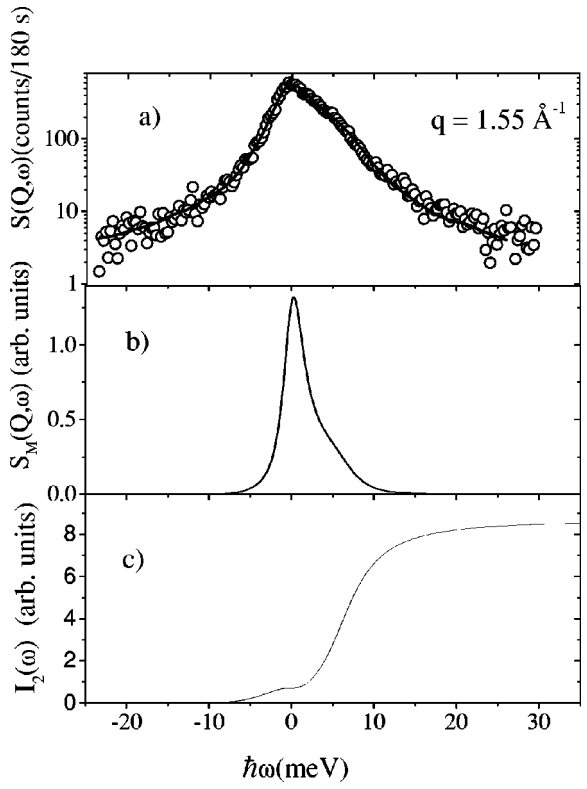

FIG. 3. (a) The IXS spectrum at $q=1.55$ Å^{-1} (open circles) together with its best fit line shape (solid line) obtained by using Eqs. (14) and (18) (total number of counts is reported). (b) The best fit model (resolution free) line shape $S_M(q,\omega)$, corresponding to the same spectrum as in (a), obtained from Eqs. (14) and (18). (c) shows, in arbitrary units, the cumulative integral $I_2(\omega)$ of Eq. (25).

The figure shows that, in the investigated spectral range, this integral reaches its convergence value.

As already said, the values of the first moment have been used to normalize the measured spectra using the *f*-sum rule. In Fig. 2 we show the reliability of this normalization comparing the values obtained from the integral of the normalized spectra with the structure factor $S(q)$ determined by neutron diffraction.[22]

Using the second-moment values obtained from the normalized spectra at low q, we can construct the second-moment ratio which we report, after subtraction of the recoil term $\hbar\omega_r$, as a function of q in Fig. 4 (solid circles) together with the corresponding high-q values (open circles) directly obtained from the fit parameters μ_2 [see Eq. (23)]. In the same figure we also report (as the solid line and dotted line) the low- and high-q limits of $[R_2(q)-\hbar\omega_r]$ given by $2K_BT$ and $\frac{4}{3}\langle \mathrm{KE}\rangle$, respectively. The quantum value of $\langle \mathrm{KE}\rangle$ has been obtained by fitting the predicted q^2 dependence of μ_2 (see inset of Fig. 4), from which we obtain $\langle \mathrm{KE}\rangle = 51 \pm 3$ K which nicely compares with the results of previous neutron measurements reported in Table I.[11–14]

Figure 4 clearly shows that the experimental data for $R_2(q)-\hbar\omega_r$ satisfy both the predicted low- and high-q limits. Both $S(q)$ and $D(q)$ are responsible for the complex behavior of $R_2(q)-\hbar\omega_r$ in between these two limits. In-

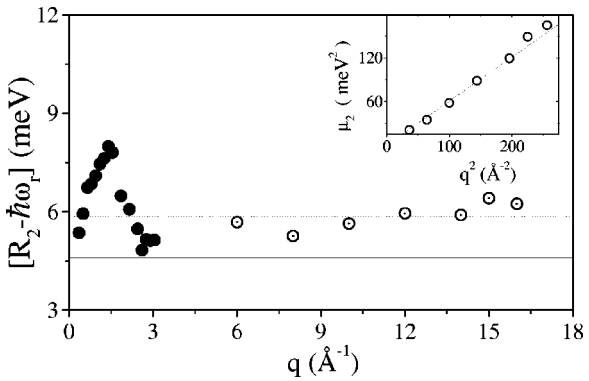

FIG. 4. The experimental values of $[R_2-\hbar\omega_r]$ (solid circles) of the low-q IXS spectra obtained from direct intensity integration are reported together with the corresponding values at high q obtained from the fitting parameter μ_2 using Eqs. (23). The solid and dashed horizontal lines represent the low-q classical expectation ($2K_BT$) and the high-q one ($4/3\langle \mathrm{KE}\rangle$), respectively. In the inset the best fit values of the parameter μ_2 of Eqs. (21) and (23) (open circles) are reported together with the parabola which best fits their q dependence, as from Eqs. (23).

deed, using the values of $S(q)$ known from neutron diffraction,[22] we can extract from our data the function $D(q)$ from Eq. (5) as reported in Fig. 5. To our knowledge, this is the first experimental determination of the kinetic structure function. The general features of this function—namely, a peak at about half of the position of the diffraction peak q_m and a pronounced shoulder around q_m—are in agreement with path integral Monte Carlo simulations of superfluid helium.[27]

The evaluation of the third-moment ratio does not require numeric integration. In fact, as already stressed [Eq. (20)], for the low-q spectra knowledge of the best fit line shape parameter ω_∞^2 of Eq. (14) provides a straightforward determination of $R_3(q)$. The values for R_3 obtained in this way are reported in Fig. 6 (solid circles). For what concerns the high-q region, $R_3(q)$ is dominated by the trivial $(\hbar\omega_r)^2$ term. In this range, a more sensible quantity to look at is directly the fitting parameter μ_3, which is reported in the

TABLE I. Average kinetic energy values for Ne at different thermodynamic points (column 3) obtained from neutron scattering experiments and from the present work (last row). The corresponding values for $\nabla^2\phi(r)$ are also reported.

T [K]	ρ [atoms/nm^2]	$\langle \mathrm{KE}\rangle$ [K]	$\langle\nabla^2\phi(r)\rangle$ [meV Å^{-2}]	Ref.
26.9	36.3	48.2±0.9	–	11
25.8	36.3	52.8±3.7	–	12
35.1	34.6	69.0±4.7	–	12
35.3	31.7	66.4±3.3	–	12
27.0	35.8	–	280±70	13
25.8	36.7	52.5±2.1	350±40	14
25.8	36.7	52.9±2.5	372±43	15
27.6	35.8	51±3	280±40	This work

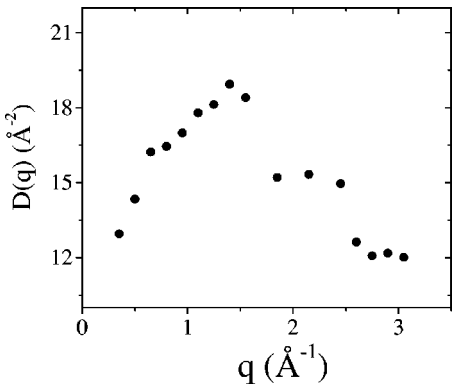

FIG. 5. The values obtained for the kinetic structure function $D(q)$ using the data of Fig. 4 together with literature data (Ref. 22) for the static structure factor $S(q)$ through Eq. (5). Note the presence of a peak in $D(q)$ at about half of the value of the first peak position q_m in the $S(q)$ and a pronounced shoulder around q_m.

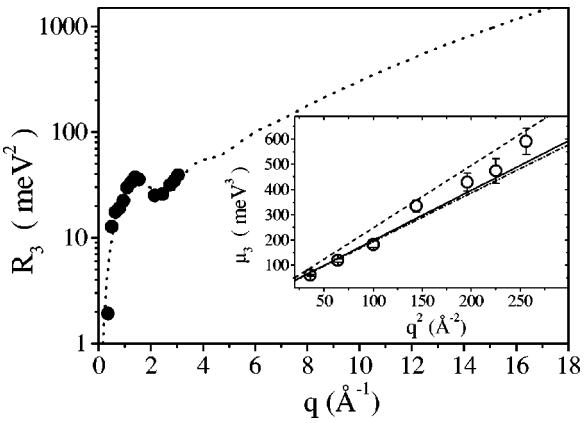

FIG. 6. The experimental values of R_3 (solid circles) are reported as a function of q; the dotted line represents the theoretical expectation worked out from Eq. (12), as specified in the text. In the inset the best fit values of the parameter μ_3 of Eqs. (21) and (23) (open circles) are reported together with their theoretical expectation (solid line) as well as with the values obtained previously using the $\langle \nabla^2 \phi(r) \rangle$ values from Refs. 13 (dash-dotted line) and 14 (dashed line). For both the R_3 and μ_3 cases, the obtained values agree well with their theoretical expectations.

inset of Fig. 6 (open circles). We can directly compare the obtained values for μ_3 with the theoretically predicted ones for $\hbar^3 \omega_r \Omega_0^2$. These have been computed by numerical integration making use of the Aziz potential[31] and using the $g(r)$ obtained from Fourier inversion of literature neutron structure factor data.[22] The results of this calculation are reported in the inset of Fig. 6 (full line). The good agreement between the experimental and theoretical values indicates the reliability of the calculated Ω_0^2 value ($\Omega_0 = 4.3$ meV). Using the calculated values of $(\Omega_0^2 - \Omega_q^2)$ and the $\langle \mathrm{KE} \rangle$ value previously determined from the q dependence of the parameter μ_2, we can also reconstruct the entire behavior of $R_3(q)$ which is reported in Fig. 6 as the dotted line. Also in this case, the results of the calculation agree well with the independent low-q determinations of $R_3(q)$. These two comparisons clearly show the reliability of the determination of the spectral moments with both line shapes used in the spectral range of validity of the models. In the inset of Fig. 6 we also report the values obtained previously using the $\langle \nabla^2 \phi(r) \rangle$ values from Refs. 13 (dash-dotted line) and 14 (dashed line). For both the R_3 and μ_3 cases, the obtained values agree well with their theoretical expectations.

V. CONCLUSIONS

In conclusion we have presented an extended inelastic x-ray scattering study of the q evolution of the dynamic structure factor of a moderately quantum fluid such as liquid neon which ranges from the quasihydrodynamic regime up to the single-particle one.

We have shown that the dynamic structure factor can be successfully described using a viscoelastic line shape model at low q's and an impulse approximation model corrected for final state effects at high q's.

From the line shape analysis of both low- and high-q spectra we were able to extract several physically meaningful quantities. In particular from the high-q spectra we can derive the mean atomic kinetic energy which turns out to be in good agreement with previous DINS measurements,[11–14] thus confirming the validity of the inelastic x-ray scattering technique in studying the high-q dynamics of simple systems.

More importantly and thanks to the possibility of investigating also the intermediate-q range, we were able not only to follow the progressive departure of the line shape from the classical towards the quantum regime, but also to derive an important quantity such as the kinetic structure function $D(q)$. This has been accomplished by studying the q dependence of different moment ratios. In particular the third-moment ratio is found to agree fairly well with the theoretical predictions based on a pairwise additive potential assumption[31] and on neutron diffraction data for the structure factor.[22] This agreement gives confidence not only in the validity of this assumption, but also in the experimental methodology that we have adopted. The second-moment ratio is found to satisfy the correct low- and high-q limits, and the transition from a classical long-range behavior to a quantum short-range behavior is clearly observed in the q range that we have accessed to.

Considering the fair overall agreement between theory and experiment and the possibility of accessing experimentally a new dynamical quantity such as the kinetic structure function, we are pursuing the project of a combined simulation-experimental study to be performed on the same quantum system.

ACKNOWLEDGMENTS

We acknowledge C. Henriquet for his technical assistance and Dr. L. Carbonara for useful discussions.

[1] V.F. Sears, Phys. Rev. B **30**, 44 (1984); S. Stringari, *ibid*. **35**, 2038 (1987); A. Miller, D. Pines, and P. Nozières, Phys. Rev. **127**, 1452 (1962); P.C. Hoenberg and P.M. Platzman, *ibid.* **152**, 198 (1966); for a comprehensive overview of the different theorethical approaches see *Moment Distribution*, edited by R.N. Silver and P.E. Sokol (Plenum, New York, 1989), and references therein.

[2] See, for example, V.F. Sears, E.C. Svensson, P. Martel, and A.D.B. Woods, Phys. Rev. Lett. **49**, 279 (1982); H.R. Glyde, R.T. Azuah, and W.G. Stirling, Phys. Rev. B **62**, 14 337 (2000).

[3] See, for example, J. Mayers, Phys. Rev. Lett. **71**, 1553 (1993).

[4] M.P. Paoli and R.S. Holt, J. Phys. C **21**, 3633 (1988).

[5] P. Verkerk, P.H.K. de Jong, M. Arai, S.M. Bennington, W.S. Howells, and A.D. Taylor, Physica B **181**, 824 (1992).

[6] C. Andreani, E. Degiorgi, R. Senesi, F. Cilloco, D. Colognesi, J. Meyers, M. Nardone, and E. Pace, J. Chem. Phys. **114**, 387 (2001).

[7] U. Balucani and M. Zoppi, *Dynamics of the Liquid State* (Clarendon Press, Oxford, 1994).

[8] V.F. Sears, Phys. Rev. A **31**, 2525 (1985).

[9] See, for example, A. Cunsolo, G. Ruocco, F. Sette, C. Masciovecchio, A. Mermet, G. Monaco, M. Sampoli, and R. Verbeni, Phys. Rev. Lett. **82**, 775 (1999).

[10] T. Scopigno, U. Balucani, A. Cunsolo, C. Masciovecchio, G. Ruocco, F. Sette, and R. Verbeni, Europhys. Lett. **50**, 189 (2000).

[11] V.F. Sears, Can. J. Phys. **63**, 68 (1985).

[12] D.A. Peek, M.C. Schmidt, I. Fujita, and R.O. Simmons, Phys. Rev. B **45**, 9671 (1992).

[13] M.A. Fradkin, S.-X. Zeng, and R.O. Simmons, Phys. Rev. B **49**, 15 563 (1994).

[14] R.T. Azuah, W.G. Stirling, H.R. Glyde, P.E. Sokol, and S.M. Bennington, Phys. Rev. B **51**, 605 (1995).

[15] R.T. Azuah, W.G. Stirling, H.R. Glyde, and M. Boninsegni, J. Low Temp. Phys. **109**, 287 (1997).

[16] R. Verbeni, A. Cunsolo, G. Pratesi, G. Monaco, F. Rosica, C. Masciovecchio, M. Nardone, G. Ruocco, F. Sette, and F. Albergamo, Phys. Rev. E **64**, 021203 (2001).

[17] G. Monaco, A. Cunsolo, G. Pratesi, F. Sette, and R. Verbeni, Phys. Rev. Lett. **88**, 227401 (2002).

[18] C. Masciovecchio, U. Bergmann, M. Krisch, G. Ruocco, F. Sette, and R. Verbeni, Nucl. Instrum. Methods Phys. Res. B **111**, 181 (1996); **117**, 339 (1996).

[19] C. Gladun, Cryogenics **6**, 27 (1966); **7**, 98 (1967).

[20] K. Carneiro and J.P. McTague, Phys. Rev. A **11**, 1744 (1975).

[21] G. Monaco, A. Cunsolo, G. Ruocco, and F. Sette, Phys. Rev. E **60**, 5505 (1999).

[22] D. Stirpe and C.W. Tompson, J. Chem. Phys. **36**, 392 (1962); D. Stirpe, Ph.D. thesis, University of Missouri, Columbia, 1961. The $S(q)$ data obtained by Stirpe and Tompson are tabulated by P.W. Schmidt and C.W. Tompson, in *Simple Dense Fluids*, edited by H.L. Frisch and Z.W. Salzburg (Academic, New York, 1968), pp. 38–39.

[23] W. Schulke, in *Handbook on Synchrotron Radiation*, edited by G. Brown and D.E. Moncton (Elsevier Science, Amsterdam, 1991), Vol. 3, pp. 565–637.

[24] See, for example, S.W. Lovesey, *Theory of Neutron Scattering from Condensed Matter* (Oxford University Press, Oxford, 1987), Vol. 1.

[25] H. Fredrikze, Mol. Phys. **48**, 993 (1983).

[26] S. Stringari, Phys. Rev. B **46**, 2974 (1992).

[27] J. Boronat, J. Casulleras, F. Dalfovo, S. Stringari, and S. Moroni, Phys. Rev. B **52**, 1236 (1995).

[28] R.D. Puff, Phys. Rev. **137**, 406 (1965).

[29] S.W. Lovesey, J. Phys. C **4**, 3057 (1971).

[30] H.R. Glyde, Phys. Rev. B **50**, 6726 (1994).

[31] R.A. Aziz, J. Meath, and A.R. Allnatt, Chem. Phys. **78**, 295 (1983).